A Galerkin-free model reduction approach for the Navier–Stokes equations

Vilas Shinde [a,*], Elisabeth Longatte [a], Franck Baj [a], Yannick Hoarau [c], Marianna Braza [b]

[a] *IMSIA, EDF–CNRS–CEA–ENSTA ParisTech UMR 9219, Clamart Cedex, France*
[b] *IMFT, Av. du prof. Camille Soula, 31400 Toulouse, France*
[c] *ICUBE, Strasbourg, France*

Keywords:
Navier–Stokes equations
Proper orthogonal decomposition
Reduced-order flow modeling
Flow control

A B S T R A C T

Galerkin projection of the Navier–Stokes equations on Proper Orthogonal Decomposition (POD) basis is predominantly used for model reduction in fluid dynamics. The robustness for changing operating conditions, numerical stability in long-term transient behavior and the pressure-term consideration are generally the main concerns of the Galerkin Reduced-Order Models (ROM). In this article, we present a novel procedure to construct an off-reference solution state by using an interpolated POD reduced basis. A linear interpolation of the POD reduced basis is performed by using two reference solution states. The POD basis functions are optimal in capturing the averaged flow energy. The energy dominant POD modes and corresponding base flow are interpolated according to the change in operating parameter. The solution state is readily built without performing the Galerkin projection of the Navier–Stokes equations on the reduced POD space modes as well as the following time-integration of the resulted Ordinary Differential Equations (ODE) to obtain the POD time coefficients. The proposed interpolation based approach is thus immune from the numerical issues associated with a standard POD-Galerkin ROM. In addition, a posteriori error estimate and a stability analysis of the obtained ROM solution are formulated. A detailed case study of the flow past a cylinder at low Reynolds numbers is considered for the demonstration of proposed method. The ROM results show good agreement with the high fidelity numerical flow simulation.

1. Introduction

Computational Fluid Dynamics (CFD) simulations are indispensable element of the engineering research today. Although there is a considerable advancement in the computing power in last couple of decades, the exact flow simulations at high Reynolds numbers are unaffordable in terms of the time and computing cost. The efforts become enormous for research applications (e.g. optimization), where the simulations need to be performed repeatedly. Consequently, reduced-order models (ROM) are developed extensively in recent years. They offer substantial reduction in the degrees of freedom and yet retaining the essential features of the flow by means of the reduced basis. The reduced system may lead to a better understanding of the underlying mechanism and thereby improvements in the empirical flow (turbulence) models. The flow

* Corresponding author.
E-mail address: vilas.shinde@polytechnique.edu (V. Shinde).

control, optimization and stability analysis in hydrodynamics, aero-acoustics are some of the potential applications of model reduction (see e.g. [17]).

The first important step of the model reduction in fluid dynamics is to form an appropriate reduced basis out of a complete set of basis functions. The choice of particular basis functions may be problem specific. The derivation of the reduced basis can be 'a priori' or 'a posteriori'. One can refer to [9,16] for some of the early works on 'a priori' formation of the basis functions. Recently, [7] used 'a priori' derivation of the basis functions, in the context of Proper General Decomposition (PGD). Besides, the spectral discretization methods are often preferred over the spatial discretization methods in order to gain the accuracy for same computing time and space requirements. In 'a posteriori' formation, the basis functions are derived using the existing solution datasets and methods such as Proper Orthogonal Decomposition (POD) (for e.g. method of Dynamic Mode Decomposition (DMD) in [21] and [22]). The POD (also Principle Component Analysis) is a popular choice of the empirical basis functions for Navier–Stokes equations. Especially, in understanding the onset of bifurcations or instabilities and the spatial–temporal dynamics of the flow structures. The error in time-averaged energy remains minimal compared to every other method for the same number of modes. The convergence in extracting the space structures (topos) and the associated time modes (chronos) is optimum in terms of the flow energy [1]. An elaborated discussion with mathematical derivations on the optimality of the POD method is provided in [8].

The POD-Galerkin ROM are build using a coordinate transformation performed by means of a Galerkin projection of the system of Navier–Stokes equations on the reduced POD basis functions. Generally, the flow velocity ($\mathbf{v}$) is decomposed into the spatial ($\boldsymbol{\phi}_i$) and temporal (a_i) basis functions as shown in Equation (1),

$$\mathbf{v}(\boldsymbol{x},t) \approx \mathbf{v}^{[0,1,2,\dots n]} = \bar{\mathbf{v}}(\boldsymbol{x}) + \sum_{i=1}^{n} \boldsymbol{\phi}_i(\boldsymbol{x}) a_i(t) \tag{1}$$

Where $\bar{\mathbf{v}}(\boldsymbol{x})$ is the time-averaged base flow, n is the number of POD modes. This equation holds good under the assumption that the flow is statistically stationary in time. In incompressible flows with Dirichlet type boundary conditions, the basis functions satisfy both the boundary conditions and the divergence-free constrain of the continuity equation. The Galerkin projection of the momentum equations on the basis functions results in the non-linear quadratic Ordinary Differential Equations (ODE) of the form:

$$\frac{da_i}{dt} = \mathbf{C}_i + \sum_{j}^{n} \mathbf{L}_{ij} a_j + \sum_{j,k}^{n} \mathbf{Q}_{ijk} a_j a_k \tag{2}$$

Where $\mathbf{C}$, $\mathbf{L}$ and $\mathbf{Q}$ are the Galerkin ROM coefficients. The indices $i, j, k = 1, \cdots, n$. Equation (2) is a reduced model for the Navier–Stokes Equations (NSE) with n spatial modes. The time-integration of Equation (2) with an appropriate initial boundary condition gives the temporal coefficients (basis functions), and the flow solution can be easily built by using Equation (1). The Galerkin projection ideally should preserve the stability dynamics of the NSE, but generally it is achieved by extrinsic stability enablers. Rempfer [19] showed how the Galerkin ROM are inherently prone to numerical instabilities. The energy associated with the truncated basis functions keeps piling on, which results in a divergence of the Galerkin-ROM. The concept of artificial viscous dissipation to stabilize the Galerkin ROM was introduced in [2]. Later, [23] proposed a spectral viscosity diffusion convolution operator based on a bifurcation analysis. In addition, the stability of Galerkin ROM greatly depends on parameters such as the flow compressibility, pressure-term consideration and time varying boundary conditions. The flow compressibility effect can be considered by means of an energy based inner product while formulating a ROM [20]. The POD-penalty method was proposed by [24] to treat the time dependence of the boundary conditions on the POD-Galerkin ROM. The Galerkin projection of the pressure-gradient term of NSE on the reduced basis functions can be neglected in case of the internal flows, but for open flows the pressure term does not disappear [18] and it needs to be modeled. The pressure term is accounted in a formulation of the pressure extended Galerkin ROM by [5]. In addition, [15] demonstrated that neglecting the interactions between the time-averaged base flow and the fluctuating flow may lead to an unstable Galerkin ROM. The authors also introduced the concept of 'shift mode' correction technique. Further, from the flow control applications point of view [14] proposed a continuous interpolation based method. In the method, an interpolation between the stability eigenmodes and the POD modes is performed to deal with the changing flow conditions. A detailed discussion on the numerical instabilities and perspectives of the reduced order models in fluid dynamics is provided by [11].

The choice of an appropriate reduced basis, the Galerkin projection of the NSE on the reduced basis and the time-integration of the obtained ODE are the main elements of the POD-Galerkin ROM. The POD basis functions are optimal in terms of flow energy, while as the Galerkin projection of NSE on the reduced basis may not produce a stable ROM as discussed above. In this article, we propose a novel approach, where it is not required to perform the Galerkin projection of NSE on the reduced basis and also the time-integration to obtain the POD time coefficients. The time-averaged base flow and the POD space basis functions (topos) are directly interpolated for the change in operating condition. The POD temporal basis functions (chronos) are also interpolated in phase space. The periodicity (the period of limit-cycles) of the POD temporal modes is accounted for the energy conservation. Furthermore, the method is extended for a continuous transition between two operating conditions. Also a linear extrapolation of the POD reduced basis is performed to widen the range of operating parameter. The article is organized as: Section 2 is dedicated to the mathematical formulation and error analysis

of the proposed ROM. In Section 3, we provide a demonstration of the method using a case study of the flow past a cylinder at low Reynolds numbers. At last, the work is summarized in Section 4.

2. Mathematical formulation

The compressible Navier–Stokes equations (including the continuity and energy equations) are considered here as the High Fidelity Model (HFM). The flow is statistically stationary in time such that Equation (1) is applicable to the solution (state) variables. The solution state vector $\boldsymbol{s} = \boldsymbol{s}(\boldsymbol{x}, t)$ is spanned on the space $\boldsymbol{x} \in \Omega$, Ω is the spacial flow domain. t is the time in $[0, T_\infty]$. Let H be a Hilbert space and a state variable $\boldsymbol{s}_i(\boldsymbol{x}, t) \in H$ with $i = 1, 2, \cdots, r(\boldsymbol{s})$. $r(\boldsymbol{s})$ is the number of state variables. The standard inner product of the state variables $\boldsymbol{s}_i(\boldsymbol{x}, t_1)$, $\boldsymbol{s}_i(\boldsymbol{x}, t_2)$ and the solution state vector $\boldsymbol{s}(\boldsymbol{x}, t)$ are respectively,

$$
\begin{aligned}
(\boldsymbol{s}_i(\boldsymbol{x}, t_1), \boldsymbol{s}_i(\boldsymbol{x}, t_2))_\Omega &= \int_\Omega \boldsymbol{s}_i(\boldsymbol{x}, t_1) \cdot \boldsymbol{s}_i(\boldsymbol{x}, t_2) d\boldsymbol{x} \\
(\boldsymbol{s}(\boldsymbol{x}, t_1), \boldsymbol{s}(\boldsymbol{x}, t_2))_\Omega &= \begin{pmatrix} (\boldsymbol{s}_i(\boldsymbol{x}, t_1), \boldsymbol{s}_i(\boldsymbol{x}, t_2))_\Omega \\ \vdots \\ \left(\boldsymbol{s}_{r(\boldsymbol{s})}(\boldsymbol{x}, t_1), \boldsymbol{s}_{r(\boldsymbol{s})}(\boldsymbol{x}, t_2)\right)_\Omega \end{pmatrix}
\end{aligned} \tag{3}
$$

The induced norm and time averaging (for time period T_∞) of a state variable and the solution state vector are respectively defined as,

$$
\begin{aligned}
||\boldsymbol{s}_i||_\Omega &= \sqrt{(\boldsymbol{s}_i, \boldsymbol{s}_i)_\Omega} \quad \text{and} \quad \bar{\boldsymbol{s}}_i = \frac{1}{T_\infty} \int_{T_\infty} \boldsymbol{s}_i \, dt = \langle \boldsymbol{s}_i \rangle_{T_\infty} \\
||\boldsymbol{s}||_\Omega &= \begin{pmatrix} \sqrt{(\boldsymbol{s}_i, \boldsymbol{s}_i)_\Omega} \\ \vdots \\ \sqrt{(\boldsymbol{s}_{r(\boldsymbol{s})}, \boldsymbol{s}_{r(\boldsymbol{s})})_\Omega} \end{pmatrix} \quad \text{and} \quad \bar{\boldsymbol{s}} = \frac{1}{T_\infty} \int_{T_\infty} \boldsymbol{s} \, dt = \langle \boldsymbol{s} \rangle_{T_\infty}
\end{aligned} \tag{4}
$$

2.1. Method of snapshots POD

The POD or Karhunen–Loeve expansion was first introduced in fluid dynamics by [12] for the analysis of coherent structures in the flow turbulence. Following the development of POD, [25] introduced the method of snapshots for the experimental and numerical datasets. It allows further reduction of degrees of freedom, compared to the direct method of POD.

The solution state vector $\boldsymbol{s}$ includes all variables varying in the time and space. Let η be an operating parameter (e.g. Reynolds number). The state vector of the High Fidelity Model (HFM) solution can be defined as,

$$
\boldsymbol{s}(\boldsymbol{x}, t; \eta) = \begin{pmatrix} \rho(\boldsymbol{x}, t; \eta) \\ \mathbf{v}(\boldsymbol{x}, t; \eta) \\ p(\boldsymbol{x}, t; \eta) \\ \vdots \end{pmatrix} \tag{5}
$$

Where ρ, $\mathbf{v}$ and p are the fluid density, velocity vector and static pressure respectively. The state vector can be separated in the time-averaged base flow and the unsteady part as shown in Equation (6).

$$
\boldsymbol{s}(\boldsymbol{x}, t; \eta) = \bar{\boldsymbol{s}}(\boldsymbol{x}; \eta) + \boldsymbol{s}'(\boldsymbol{x}, t; \eta) \tag{6}
$$

$$
= \bar{\boldsymbol{s}}(\boldsymbol{x}; \eta) + \sum_{i=1}^{\infty} \boldsymbol{\phi}_i(\boldsymbol{x}; \eta) \boldsymbol{a}_i(t; \eta) \tag{7}
$$

In Equation (7), the unsteady part ($\boldsymbol{s}'(\boldsymbol{x}, t; \eta)$) is decomposed into the POD basis functions using the Galerkin expansion. The time invariant orthonormal $\boldsymbol{\phi}_i(\boldsymbol{x}; \eta)$ and the space invariant orthogonal $\boldsymbol{a}_i(t; \eta)$ are the POD basis functions (modes). The state vector can be obtained in discrete (N_t) snapshots by performing a CFD simulation. The snapshots can be collected once the flow becomes statistically stationary and using (typically) a constant timestep (Δt_{sn}). Let N_t, N_{pod} be the number of snapshots and number of POD modes respectively, also $N_{pod} \leq N_{t-1}$. The state vector can be approximated by discrete snapshots as,

$$
\boldsymbol{s}(\boldsymbol{x}, t; \eta) \approx \boldsymbol{s}(\boldsymbol{x}, t_1; \eta), \ldots, \boldsymbol{s}(\boldsymbol{x}, t_{N_t}; \eta) \tag{8}
$$

$$
\approx \bar{\boldsymbol{s}}(\boldsymbol{x}; \eta) + \sum_{i=1}^{N_{pod}} \boldsymbol{\phi}_i(\boldsymbol{x}; \eta) \boldsymbol{a}_i(t; \eta) \quad t_1 \leq t \leq t_{N_t} \tag{9}
$$

Where t_1 and t_{N_t} are the time coordinates of the first and last snapshots. Also, let $T_{sn} = [t_1, .., t_{N_t}]$ be the time domain of discrete snapshots collection. The time step (Δt_{sn}) of snapshots recording and the number of snapshots (N_t) depend on the desired resolution in the temporal harmonics of the POD modes [18].

Let $\boldsymbol{R}(\eta)$ be the two point time-correlation function, given by,

$$\boldsymbol{R}(\eta) = \boldsymbol{R}(t_i, t_j, \eta) = \frac{1}{N_t} \left(\boldsymbol{s}'(\boldsymbol{x}, t_i; \eta), \boldsymbol{s}'(\boldsymbol{x}, t_j; \eta)\right)_\Omega \quad i, j = 1, 2, \ldots N_t \tag{10}$$

The correlation function $\boldsymbol{R}(\eta)$ is solved for the eigenvalue problem, as in Equation (12).

$$\boldsymbol{R}(\eta)\boldsymbol{\psi}_i(t; \eta) = \boldsymbol{\lambda}_i \boldsymbol{\psi}_i(t; \eta) \tag{11}$$

where $\boldsymbol{\lambda}_i$ are the eigenvalues. The orthogonal eigenfunctions $\boldsymbol{\psi}_i(t; \eta)$ are then normalized as,

$$\left(\boldsymbol{\psi}_i(t; \eta), \boldsymbol{\psi}_j(t; \eta)\right)_{T_{sn}} = \boldsymbol{\delta}_{ij} \tag{12}$$

Where, $\boldsymbol{\delta}_{ij}$ is the Kronecker delta in vector form. The POD modes are arranged in descending order of their energy content (the eigenvalues associated with the modes), i.e. $\boldsymbol{\lambda}_1 > \boldsymbol{\lambda}_2 > \ldots > \boldsymbol{\lambda}_{N_{pod}} > 0$. The orthonormal 'topos' are obtained using Equation (13), such that $\left(\boldsymbol{\phi}_i(\boldsymbol{x}; \eta), \boldsymbol{\phi}_i(\boldsymbol{x}; \eta)\right)_\Omega = \boldsymbol{\delta}_{ij}$.

$$\boldsymbol{\phi}_i(\boldsymbol{x}; \eta) = \frac{1}{\sqrt{N_t \boldsymbol{\lambda}_i}} \left(\boldsymbol{s}'(\boldsymbol{x}, t; \eta), \boldsymbol{\psi}_i(t; \eta)\right)_{T_{sn}} \tag{13}$$

The corresponding POD time coefficients are given by,

$$\begin{aligned} \boldsymbol{a}_i(t; \eta) &= \left(\boldsymbol{\phi}_i(\boldsymbol{x}; \eta), \boldsymbol{s}'(\boldsymbol{x}, t; \eta)\right)_\Omega \\ &= \sqrt{N_t \boldsymbol{\lambda}_i} \boldsymbol{\psi}_i(t; \eta) \end{aligned} \tag{14}$$

Generally, the number of reduced POD modes (N_r) is much smaller compared to the total POD modes ($N_r << N_{pod}$). The relative energy captured ($\boldsymbol{Ec}$) by the most energetic (first few) POD modes is substantial. It can be given as,

$$\%\boldsymbol{Ec} = \frac{\sum_{i=1}^{N_r} \boldsymbol{\lambda}_i}{\sum_{i=1}^{N_{pod}} \boldsymbol{\lambda}_i} \times 100 \tag{15}$$

2.2. Periodicity of POD temporal modes

The total energy[1] $\boldsymbol{E}(\eta)_{pod}$ of the unsteady part of the discrete state vector can be given by,

$$\boldsymbol{E}(\eta)_{pod} = \frac{1}{2} \int_\Omega \left\langle \boldsymbol{s}'(\boldsymbol{x}, t, \eta)^2 \right\rangle_{T_{sn}} d\boldsymbol{x} = \frac{1}{2} \sum_{i=1}^{N_{pod}} \boldsymbol{\lambda}_i = \frac{1}{2} \sum_{i=1}^{N_{pod}} \left\langle \boldsymbol{a}_i(t; \eta)^2 \right\rangle_{T_{sn}} \tag{16}$$

The space domain (Ω) is limited by a boundary ($\partial\Omega$). Similarly, let T_{min} be the minimum time window for which the total energy in Equation (16) remains the same, such that,

$$\boldsymbol{E}(\eta)_{pod} = \frac{1}{2} \int_\Omega \left\langle \boldsymbol{s}'(\boldsymbol{x}, t, \eta)^2 \right\rangle_{T_{min}} d\boldsymbol{x} = \frac{1}{2} \sum_{i=1}^{N_{pod}} \boldsymbol{\lambda}_i = \frac{1}{2} \sum_{i=1}^{N_{pod}} \left\langle \boldsymbol{a}_i(t; \eta)^2 \right\rangle_{T_{min}} \tag{17}$$

In statistically stationary flows, the POD temporal basis functions observe the stable limit cycles in phase space (see for e.g. [23,13,1]). Let T_η be the time period of the limit-cycle of first POD time coefficient $\boldsymbol{a}_1(t; \eta)$. The higher (well resolved by snapshots) POD time modes for the state vector are periodic with the time T_η. The characteristic POD time coefficients can be defined as,

$$\tilde{\boldsymbol{a}}_i(t; \eta) = \boldsymbol{a}_i(t; \eta) \quad \text{for } t \in [t_a, t_a + T_\eta] \tag{18}$$

Where $t_a \in \left[0, (T_{sn} - T_\eta)\right]$ is an arbitrary time. Further, the total energy in Equation (17) becomes,

$$\boldsymbol{E}(\eta)_{pod} = \frac{1}{2} \sum_{i=1}^{N_{pod}} \left\langle \tilde{\boldsymbol{a}}_i(t; \eta)^2 \right\rangle_{T_\eta} = \frac{1}{2} \sum_{i=1}^{N_{pod}} \left\langle \boldsymbol{a}_i(t; \eta)^2 \right\rangle_{T_{min}} = \frac{1}{2} \sum_{i=1}^{N_{pod}} \boldsymbol{\lambda}_i \tag{19}$$

[1] An appropriate term for the non-velocity variables (e.g. density, pressure) be the 'variance'.

It also implies that the minimum time window (T_{min}) is the time period of the first POD temporal mode (T_η).

Under the statistically stationary flow assumption and using the periodic characteristic POD temporal modes (Equation (18)), one can reconstruct the flow with reduced number (N_r) of POD basis even outside the snapshots time domain (T_{sn}) as,

$$\boldsymbol{s}(\boldsymbol{x}, t; \eta) \approx \bar{\boldsymbol{s}}(\boldsymbol{x}; \eta) + \sum_{i=1}^{N_r} \boldsymbol{\phi}_i(\boldsymbol{x}; \eta)\tilde{\boldsymbol{a}}_i(t; \eta) \quad t \geq 0 \tag{20}$$

2.3. Linear interpolation

A linear interpolation is used to interpolate the right hand side terms of Equation (20) for the change in operating parameter η. The interpolation of the characteristic POD temporal modes ($\tilde{\boldsymbol{a}}_i$) ensures the appropriate flow energy ($\boldsymbol{E}(\eta)$) levels in the interpolated state.

Let $\boldsymbol{s}(\boldsymbol{x}, t; \eta_j)$ with $j = 1, 2$ be the two reference states. In order to build a solution state vector at an operating parameter $\eta \in [\eta_1, \eta_2]$, the time-averaged base flow $\bar{\boldsymbol{s}}(\boldsymbol{x}; \eta)$, the POD spacial modes ($\boldsymbol{\phi}_i(\boldsymbol{x}; \eta)$) and the associated time coefficients $\tilde{\boldsymbol{a}}_i(t; \eta)$ are obtained by the linear interpolation of the reference states. The interpolation is formulated using a vector $\boldsymbol{\Gamma}(\boldsymbol{\beta}; \eta)$ in Equation (21). It stands for the solution state average ($\bar{\boldsymbol{s}}(\boldsymbol{x}; \eta)$) and the POD modes ($\boldsymbol{\phi}_i(\boldsymbol{x}; \eta)$ and $\tilde{\boldsymbol{a}}_i(t; \eta)$).

$$\boldsymbol{\Gamma}(\boldsymbol{\beta}; \eta) = \boldsymbol{\Gamma}(\boldsymbol{\beta}; \eta_1) + \left[\frac{(\boldsymbol{\Gamma}(\boldsymbol{\beta}; \eta_2) - \boldsymbol{\Gamma}(\boldsymbol{\beta}; \eta_1))}{(\eta_2 - \eta_1)}\right](\eta - \eta_1) \tag{21}$$

Here $\boldsymbol{\beta}$ is either $\boldsymbol{x}$, for $\bar{\boldsymbol{s}}$, $\boldsymbol{\phi}_i$ or $t \in [0, T_\eta]$ for $\tilde{\boldsymbol{a}}_i$. A priori, the condition in Equation (22) is satisfied so that the interpolated quantities (RHS of Equation (20)) follow the signs of any of the two (η_1 and η_2) reference cases.

$$(\boldsymbol{\Gamma}(\boldsymbol{\beta}; \eta_1), \boldsymbol{\Gamma}(\boldsymbol{\beta}; \eta_2))_{\boldsymbol{\beta}} \geq 0 \tag{22}$$

The time-averages of the state vectors ($\bar{\boldsymbol{s}}(\boldsymbol{x}; \eta_j)$ for $j = 1, 2$) generally do not alter their sign for the change in operating parameter (η_j). A symmetry in the flow geometry can lead to a phase difference of π between the corresponding POD space modes ($\boldsymbol{\phi}_i(\boldsymbol{x}; \eta_j)$) for different operating conditions (η_j). The constrain in Equation (22) ensures that they do not cancel out, while performing the interpolation. In addition, the reference states η_j need to be close enough, in order to perform the linear interpolation (Equation (21)). The characteristic POD time coefficients ($\tilde{\boldsymbol{a}}_i(t; \eta)$) are brought in minimal phase difference by using Equation (22). The interpolated base solution and the POD modes follow any one of the reference states for the phase. The characteristic time period (T_η) is also linearly interpolated for the change in operating parameter (η). The interpolation ROM solution, with the reduced number (N_r) of POD interpolated basis and for the change of parameter (η) in $[\eta_1, \eta_2]$, can be written as,

$$\boldsymbol{s}(\boldsymbol{x}, t; \eta) \approx \bar{\boldsymbol{s}}(\boldsymbol{x}; \eta) + \sum_{i=1}^{N_r} \boldsymbol{\phi}_i(\boldsymbol{x}; \eta)\tilde{\boldsymbol{a}}_i(t; \eta) \quad t \geq 0 \;\&\; \eta \in [\eta_1, \eta_2] \tag{23}$$

A smooth transition of a ROM solution from one flow state to another is useful in the flow control applications. A continuous mode interpolating technique developed in [14] uses a parameter κ for a continuous transition between the stability matrices at a steady state to an unsteady (with periodic limit cycle) state. Similarly, a smooth transition between two interpolated off-reference states (η^n, η^{n+1}) can be achieved by,

$$\boldsymbol{\Gamma}(\boldsymbol{\beta}; \eta^{n+1}) = \kappa\boldsymbol{\Gamma}(\boldsymbol{\beta}; \eta^{n+1}) + (1 - \kappa)\boldsymbol{\Gamma}(\boldsymbol{\beta}; \eta^n) \tag{24}$$

$$T_{\eta^{n+1}} = \kappa T_{\eta^{n+1}} + (1 - \kappa)T_{\eta^n} \tag{25}$$

Here n is an integer indicator for a flow state. The transition parameter κ varies from 0 to 1. A simple linear function with an appropriate time delay parameter (c_τ) can be used to obtain a real time transition. Equation (26) shows such a function.

$$\kappa = c_\tau \left(t - t_0^{n+1}\right) / T_{\eta^{n+1}} \tag{26}$$

Where, t_0^{n+1} represents the time of control parameter change. The time delay constant (c_τ) can be used to control the transition time.

In addition to the linear interpolation, a linear extrapolation of the reference states (η_1 and η_2) can also be used to widen the range of controlling parameter, with a caution of the presence of major flow transitions in the vicinity.

2.4. A posteriori error estimate

2.4.1. Snapshots POD and truncation errors

The High Fidelity Model (HFM) solution can be an accurate CFD solution to the full NSEs or the experimental datasets for the flow under consideration. The HFM solution state vector can be expressed in terms of POD basis functions by Equation (7). The method of snapshots leads to an approximation (similar to Equation (9)),

$$\boldsymbol{s}(\boldsymbol{x},t;\eta)_{hf} \approx \bar{\boldsymbol{s}}(\boldsymbol{x};\eta)_{pod} + \sum_{i=1}^{N_{pod}} \boldsymbol{\phi}_i(\boldsymbol{x};\eta)_{pod}\tilde{\boldsymbol{a}}_i(t;\eta)_{pod} \tag{27}$$

The subscript '*hf*' stands for a high fidelity solution, while as the subscript '*pod*' stands for quantities estimated using POD. A posteriori the error in POD discretization can be given by,

$$\boldsymbol{\epsilon}_{p\boldsymbol{s}}(\boldsymbol{x},t;\eta) = \boldsymbol{s}(\boldsymbol{x},t;\eta)_{hf} - \boldsymbol{s}(\boldsymbol{x},t;\eta)_{pod} \tag{28}$$

Where the subscript '$p\boldsymbol{s}$' stands for a POD based error in the solution state vector $\boldsymbol{s}$. The POD error depends mainly on the timestep of snapshots collection (ΔT_{sn}), number of snapshots (N_t) and the time-window of snapshots collection (T_{sn}). A rigorous parametric analysis and error estimate study of the POD method was performed by Kunisch and Volkwein [10]. In order to normalize the errors, let us represent the element wise division of vectors $\boldsymbol{u}$ and $\boldsymbol{v}$ as $\boldsymbol{u} \oslash \boldsymbol{v}$, for no element of vector $\boldsymbol{v}$ is zero ($v_i \neq 0$). Further, the total variance can be defined for the high fidelity state vector $\boldsymbol{s}(\boldsymbol{x},t;\eta)$ as,

$$\boldsymbol{\sigma}^2(\eta) = \int_{\Omega} \left\langle \boldsymbol{s}'(\boldsymbol{x},t;\eta)^2_{hf} \right\rangle_{T_\infty} d\boldsymbol{x} \tag{29}$$

A posteriori, normalized error in POD discretization can be given by,

$$\epsilon_p(t;\eta) = \left\| \int_{\Omega} \boldsymbol{\epsilon}_{p\boldsymbol{s}}(\boldsymbol{x},t;\eta)^2 d\boldsymbol{x} \oslash \boldsymbol{\sigma}^2(\eta) \right\|_{r(\boldsymbol{s})} \tag{30}$$

In addition, the error introduced by the truncation of the higher ($> N_r$) POD modes can be obtained as,

$$\boldsymbol{\epsilon}_{t\boldsymbol{s}}(\boldsymbol{x},t;\eta) = \sum_{i=N_r+1}^{N_{pod}} \boldsymbol{\phi}_i(\boldsymbol{x};\eta)_{pod}\, \tilde{\boldsymbol{a}}_i(t;\eta)_{pod} \tag{31}$$

The normalized truncation error becomes,

$$\epsilon_t(t;\eta) = \left\| \int_{\Omega} \boldsymbol{\epsilon}_{t\boldsymbol{s}}(\boldsymbol{x},t;\eta)^2 d\boldsymbol{x} \oslash \boldsymbol{\sigma}^2(\eta) \right\|_{r(\boldsymbol{s})} \tag{32}$$

2.4.2. Interpolation error

The interpolation errors associated with each term of the ROM solution (Equation (23)) with respect to the POD solution can be defined,

$$\begin{aligned}
\boldsymbol{\epsilon}_{\bar{\boldsymbol{s}}}(\boldsymbol{x};\eta) &= \bar{\boldsymbol{s}}(\boldsymbol{x};\eta)_{pod} - \bar{\boldsymbol{s}}(\boldsymbol{x};\eta) \\
\boldsymbol{\epsilon}_{\boldsymbol{\phi}_i}(\boldsymbol{x};\eta) &= \boldsymbol{\phi}_i(\boldsymbol{x};\eta)_{pod} - \boldsymbol{\phi}_i(\boldsymbol{x};\eta) \\
\boldsymbol{\epsilon}_{\tilde{\boldsymbol{a}}_i}(t;\eta) &= \tilde{\boldsymbol{a}}_i(t;\eta)_{pod} - \tilde{\boldsymbol{a}}_i(t;\eta)
\end{aligned} \tag{33}$$

Let $\boldsymbol{\epsilon}_{i\boldsymbol{s}}(\boldsymbol{x},t;\eta)$ be the total interpolation error in solution state vector ($\boldsymbol{s}$) with respect to the POD solution. It can be given as,

$$\boldsymbol{\epsilon}_{i\boldsymbol{s}}(\boldsymbol{x},t;\eta) = \boldsymbol{s}(\boldsymbol{x},t;\eta)_{pod} - \boldsymbol{s}(\boldsymbol{x},t;\eta) \tag{34}$$

$$\boldsymbol{\epsilon}_{i\boldsymbol{s}}(\boldsymbol{x},t;\eta) = \left(\bar{\boldsymbol{s}}(\boldsymbol{x};\eta)_{pod} + \sum_{i=1}^{N_r} \boldsymbol{\phi}_i(\boldsymbol{x};\eta)_{pod}\tilde{\boldsymbol{a}}_i(t;\eta)_{pod} \right) - \left(\bar{\boldsymbol{s}}(\boldsymbol{x};\eta) + \sum_{i=1}^{N_r} \boldsymbol{\phi}_i(\boldsymbol{x};\eta)\tilde{\boldsymbol{a}}_i(t;\eta) \right) \tag{35}$$

Using the individual error definitions from Equation (33) and the total interpolation error in Equation (35) we obtain,

$$\boldsymbol{\epsilon}_{i\boldsymbol{s}}(\boldsymbol{x},t;\eta) = \boldsymbol{\epsilon}_{\bar{\boldsymbol{s}}}(\boldsymbol{x};\eta) + \sum_{i=1}^{N_r} \boldsymbol{\phi}_i(\boldsymbol{x};\eta)\boldsymbol{\epsilon}_{\tilde{\boldsymbol{a}}_i}(t;\eta) + \boldsymbol{\epsilon}_{\boldsymbol{\phi}_i}(\boldsymbol{x};\eta)\tilde{\boldsymbol{a}}_i(t;\eta) + \boldsymbol{\epsilon}_{\boldsymbol{\phi}_i}(\boldsymbol{x};\eta)\boldsymbol{\epsilon}_{\tilde{\boldsymbol{a}}_i}(t;\eta) \tag{36}$$

A priori, the maximum error bound in the linear interpolation can be given by Equation (37), for each interpolation error term from Equation (36). The second derivatives ($\boldsymbol{\alpha}_*$) must exist.

$$|\boldsymbol{\epsilon}_{\bar{\boldsymbol{s}}}(\boldsymbol{x};\eta)| \leq \frac{1}{8}(\Delta\eta)^2 \sup_{\eta\in[\eta_1,\eta_2]} |\boldsymbol{\alpha}_{\bar{\boldsymbol{s}}}(\boldsymbol{x};\eta)| \quad \text{where } \boldsymbol{\alpha}_{\bar{\boldsymbol{s}}}(\boldsymbol{x};\eta) = \frac{\partial^2}{\partial\eta^2}(\bar{\boldsymbol{s}}(\boldsymbol{x};\eta)_{pod})$$

$$\left|\boldsymbol{\epsilon}_{\boldsymbol{\phi}_i}(\boldsymbol{x};\eta)\right| \leq \frac{1}{8}(\Delta\eta)^2 \sup_{\eta\in[\eta_1,\eta_2]} \left|\boldsymbol{\alpha}_{\boldsymbol{\phi}_i}(\boldsymbol{x};\eta)\right| \quad \text{where } \boldsymbol{\alpha}_{\boldsymbol{\phi}_i}(\boldsymbol{x};\eta) = \frac{\partial^2}{\partial\eta^2}(\boldsymbol{\phi}_i(\boldsymbol{x};\eta)_{pod})$$

$$\left|\boldsymbol{\epsilon}_{\tilde{\boldsymbol{a}}_i}(t;\eta)\right| \leq \frac{1}{8}(\Delta\eta)^2 \sup_{\eta\in[\eta_1,\eta_2]} \left|\boldsymbol{\alpha}_{\tilde{\boldsymbol{a}}_i}(t;\eta)\right| \quad \text{where } \boldsymbol{\alpha}_{\tilde{\boldsymbol{a}}_i}(t;\eta) = \frac{\partial^2}{\partial\eta^2}(\tilde{\boldsymbol{a}}_i(t;\eta)_{pod}) \tag{37}$$

The error is $\mathcal{O}(\Delta\eta^2)$. Here $\Delta\eta = (\eta_2 - \eta_1)$. The value of $\Delta\eta$ can be chosen based on the total interpolation error bound $|\boldsymbol{\epsilon}_{i\boldsymbol{s}}(\boldsymbol{x},t;\eta)|$. The total interpolation error in the solution state vector $\boldsymbol{s}(\boldsymbol{x},t;\eta)$ is in bounds as,

$$|\boldsymbol{\epsilon}_{i\boldsymbol{s}}(\boldsymbol{x},t;\eta)| \leq \frac{1}{8}(\Delta\eta)^2 \sup_{\eta\in[\eta_1,\eta_2]} \left| \boldsymbol{\alpha}_{\bar{\boldsymbol{s}}}(\boldsymbol{x};\eta) + \sum_{i=1}^{N_r} \boldsymbol{\phi}_i(\boldsymbol{x};\eta)\boldsymbol{\alpha}_{\tilde{\boldsymbol{\alpha}}_i}(t;\eta) + \right.$$
$$\left. \boldsymbol{\alpha}_{\boldsymbol{\phi}_i}(\boldsymbol{x};\eta)\tilde{\boldsymbol{a}}_i(t;\eta) + \frac{1}{8}(\Delta\eta)^2\boldsymbol{\alpha}_{\boldsymbol{\phi}_i}(\boldsymbol{x};\eta)\boldsymbol{\alpha}_{\tilde{\boldsymbol{\alpha}}_i}(t;\eta) \right| \tag{38}$$

On the other hand, a posteriori interpolation error can be directly given by Equation (34). The normalized interpolation error will be,

$$\epsilon_i(t;\eta) = \left|\left| \int_\Omega \boldsymbol{\epsilon}_{i\boldsymbol{s}}(\boldsymbol{x},t;\eta)^2 d\boldsymbol{x} \oslash \boldsymbol{\sigma}^2(\eta) \right|\right|_{r(\boldsymbol{s})} \tag{39}$$

2.4.3. Energy based error

Generally, the error in Galerkin ROM is quantified based on the quadratic flow energy terms. The POD basis functions (topos and chronos) are the optimal basis for a ROM in fluid dynamics, hence it provides an upper bound for the error in Gelerkin ROM [3,6]. The normalized error in ROM based on the kinetic energy can be expressed as,

$$\begin{aligned}\epsilon_e(t;\eta) &= \left|\left| \left(\boldsymbol{E}(t;\eta)_{pod} - \boldsymbol{E}(t;\eta)\right) \oslash \boldsymbol{\sigma}^2(\eta) \right|\right|_{r(\boldsymbol{s})} \\ &= \left|\left| \left(\sum_{i=1}^{N_{pod}} \tilde{\boldsymbol{a}}_i(t;\eta)^2_{pod} - \sum_{i=1}^{N_r} \tilde{\boldsymbol{a}}_i(t;\eta)^2 \right) \oslash \boldsymbol{\sigma}^2(\eta) \right|\right|_{r(\boldsymbol{s})}\end{aligned} \tag{40}$$

Where $\boldsymbol{E}(t;\eta)$ is the energy of ROM solution. In the presented formulation of ROM, the energy based error ($\epsilon_e(t;\eta)$) does not account for the error in interpolation of the time-averaged base flow ($\bar{\boldsymbol{s}}(\boldsymbol{x};\eta)$) as well as the POD space modes ($\boldsymbol{\phi}_i(\boldsymbol{x};\eta)$). Therefore the total error relevant to the interpolation ROM can be defined as,

$$\epsilon_{it}(t;\eta) = \epsilon_i(t;\eta) + \epsilon_t(t;\eta) \tag{41}$$

2.5. Stability of the interpolation ROM

Almost all the Galerkin ROM are unstable and need stabilization techniques such as addition of the artificial viscosity terms, increasing the order of ROM. This way, either the high fidelity Navier–Stokes equation are altered or the computational efforts are increased [3]. On the contrary, the interpolation based approach of ROM uses the flow statistical stationarity assumption for the energy balance instead of balancing the energy of truncated POD modes by means of the empirical turbulence models. The time average of the total error $\epsilon_{it}(t;\eta)$ in the interpolation ROM (Equation (41)) can be given by,

$$\epsilon(\eta) = \langle \epsilon_{it}(t;\eta) \rangle_{T_\infty} = \langle \epsilon_{it}(t;\eta) \rangle_{T_\eta} \tag{42}$$

it implies,

$$\frac{\partial\epsilon(\eta)}{\partial T_\eta} = 0 \tag{43}$$

The errors ($\boldsymbol{\epsilon}_{p\boldsymbol{s}}(\boldsymbol{x},t;\eta)$, $\boldsymbol{\epsilon}_{t\boldsymbol{s}}(\boldsymbol{x},t;\eta)$ and $\boldsymbol{\epsilon}_{i\boldsymbol{s}}(\boldsymbol{x},t;\eta)$) in the interpolation ROM are in bounds under the stationary flow assumption for all time. The total normalized error $\epsilon(\eta)$ remains a function of the parameters ΔT_{sn}, N_t, N_{pod}, N_r, $\Delta\eta$ and the second derivatives $\boldsymbol{\alpha}_{\bar{\boldsymbol{s}}}$, $\boldsymbol{\alpha}_{\boldsymbol{\phi}_i}$ and $\boldsymbol{\alpha}_{\tilde{\boldsymbol{a}}_i}$.

2.5.1. Floquet stability analysis

Let N_o be the number of POD time modes with the time period T_η. The periodic base flow for the Floquet instability can be given as,

$$\boldsymbol{s}_o(\boldsymbol{x}, t; \eta) = \bar{\boldsymbol{s}}(\boldsymbol{x}; \eta) + \sum_{i=1}^{N_o} \boldsymbol{\phi}_i(\boldsymbol{x}; \eta)\boldsymbol{a}_i(t; \eta) \tag{44}$$

Let $\boldsymbol{s}'_o(\boldsymbol{x}, t; \eta)$ be the small perturbation in the base flow. It is can be represented in terms of the POD basis as,

$$\boldsymbol{s}'_o(\boldsymbol{x}, t; \eta) \approx \sum_{i=N_o+1}^{N_r} \chi_i = \sum_{i=N_o+1}^{N_r} \boldsymbol{\phi}_i(\boldsymbol{x}; \eta)\boldsymbol{a}_i(t; \eta) \tag{45}$$

The perturbation $\boldsymbol{s}'_o(\boldsymbol{x}, t; \eta)$ in the base flow is periodic with the period T_η. Therefore we can consider Equation (45) for the Floquet analysis. The T_η periodic functions χ_i can be represented in the form, $\tilde{\chi}_i \exp(\varsigma_i t)$. Where $\tilde{\chi}_i$ are also T_η periodic and known as Floquet modes. The exponents ς_i are called the Floquet exponents. Generally, the Floquet multipliers $\xi_i \equiv \exp(\varsigma_i T_\eta)$ are used in the stability analysis. The perturbation $(\boldsymbol{s}'_o(\boldsymbol{x}, t; \eta))$ grows exponentially for $|\xi_i| > 1$ and the periodic base flow is unstable. On the other hand the perturbation decays exponentially for $|\xi_i| < 1$ and the periodic base flow is stable [4].

The Floquet modes $(\tilde{\chi}_i)$ at a time instance after n time periods (T_η) can be written as,

$$\tilde{\chi}_i^n = \boldsymbol{\phi}_i(\boldsymbol{x}; \eta)\tilde{\boldsymbol{a}}_i(t; \eta)^n \tag{46}$$

Where, $\tilde{\boldsymbol{a}}_i(t; \eta)^n = \tilde{\boldsymbol{a}}_i(t_0 + nT_\eta; \eta)$ are the POD time modes at n time periods (T_η) after an initial time t_0. The characteristic POD time modes, as defined in Equation (18), are periodic with time T_η. Therefore $\tilde{\boldsymbol{a}}_i(t_0 + nT_\eta; \eta) = \tilde{\boldsymbol{a}}_i(t_0 + (n+1)T_\eta; \eta)$, which leads to $\tilde{\chi}_i^n = \tilde{\chi}_i^{n+1}$. Furthermore, the number of POD modes (N_r) used to build the ROM solution follow stable limit cycles with time period T_η. Thus the value of Floquet multipliers $|\xi_i| = 1$ and the corresponding Floquet exponents $\varsigma_i = 0$. The perturbation $\boldsymbol{s}'_o(\boldsymbol{x}, t; \eta)$ neither grows nor decays with the time at a particular operating condition (η).

3. Flow past a cylinder at low Reynolds number – a case study

The flow past a cylinder at low Reynolds number ($Re = 125 \sim 150$) in 2-dimension (2D) is considered for the demonstration of the proposed Reduced-Order Model (ROM). Fig. 1 shows the flow domain and the instantaneous flow fields (u, v and p) at Reynolds number $Re = 125$ ($Re = \rho u_\infty D/\mu$). The cylinder of diameter $D = 1$ is at the center of the computational domain. The inflow streamwise (along $+x$ axis) velocity (u_∞) as well as the temperature (θ_∞) far upstream are set to 1. The density of the fluid (calorically perfect gas) is $\rho = 1$. The Mach number upstream is $M_\infty = 0.18$, while as the specific heat ratio of 1.4 (for air) is taken. The gas constant R and the inflow pressure p_∞ are 22.05. The dynamic viscosity (μ) is constant, it is estimated using the Reynolds number (Re_∞) as, $\mu = (\rho \mathbf{v}_\infty D)/(Re_\infty)$. The inflow transverse velocity is $v_\infty = 0$. The internal energy (e) and the enthalpy (h) are given by $C_v\theta$ and $C_p\theta$ respectively, where C_v, C_p are the specific heats at constant volume and constant pressure respectively. The total energy (E) and the internal energy (e) are related by

$$e = E - \frac{1}{2}\left(u^2 + v^2\right))$$

3.1. Governing flow equations and numerical methods

A compressible Navier–Stokes flow solver (Navier–Stokes Multi-Block – NSMB) is used with a preconditioning for the incompressible flow at low Mach number. The NSMB solver is developed in collaboration between several European organizations which mainly includes Airbus, KTH, EPFL, IMFT, ICUBE, CERFACS, University of Karlsruhe and ETH-Ecole Polytechnique de Zurich. The code has been developed since early 90s. It is coordinated by CFS Engineering in Lausanne, Switzerland. NSMB is a structured code including a variety of high-order numerical schemes and turbulence modeling such as LES, URANS, RANS-LES hybrid turbulence modeling, especially DDES (Delayed Detached Eddy Simulations).

The compressible unsteady Navier–Stokes equations in 2D can be written as,

$$\frac{\partial}{\partial t}(\boldsymbol{w}) + \frac{\partial}{\partial x}(\boldsymbol{f} - \boldsymbol{f}_v) + \frac{\partial}{\partial y}(\boldsymbol{g} - \boldsymbol{g}_v) = 0 \tag{47}$$

Where,

$$\boldsymbol{w} = \begin{pmatrix} \rho \\ \rho u \\ \rho v \\ \rho E \end{pmatrix}, \boldsymbol{f} = \begin{pmatrix} \rho u \\ \rho u^2 + p \\ \rho uv \\ u(\rho E + p) \end{pmatrix}, \boldsymbol{g} = \begin{pmatrix} \rho v \\ \rho vu \\ \rho v^2 + p \\ v(\rho E + p) \end{pmatrix}$$

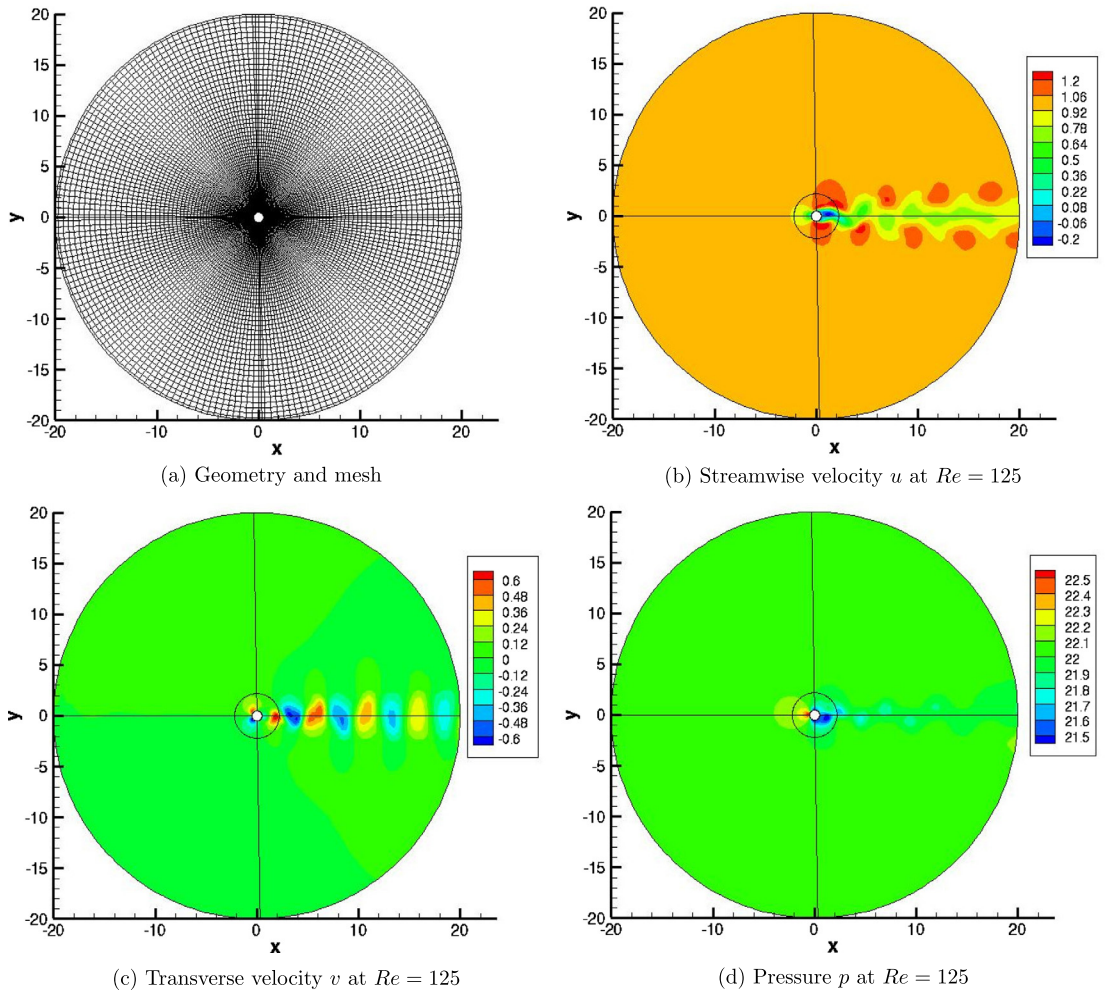

(a) Geometry and mesh

(b) Streamwise velocity u at $Re = 125$

(c) Transverse velocity v at $Re = 125$

(d) Pressure p at $Re = 125$

Fig. 1. Computational domain and instantaneous flow fields at $Re = 125$.

$$\boldsymbol{f}_v = \begin{pmatrix} 0 \\ \tau_{xx} \\ \tau_{xy} \\ [\boldsymbol{\tau}, \mathbf{v}]_x - q_x \end{pmatrix}, \boldsymbol{g}_v = \begin{pmatrix} 0 \\ \tau_{yx} \\ \tau_{yy} \\ [\boldsymbol{\tau}, \mathbf{v}]_y - q_y \end{pmatrix}$$

Here $\boldsymbol{w}$ is the state vector. $\boldsymbol{f}$, $\boldsymbol{g}$ are the convective fluxes, while as $\boldsymbol{f}_v$, $\boldsymbol{g}_v$ are the viscous fluxes. The components of shear stress tensor $\boldsymbol{\tau}$ in the viscous fluxes are given by Equation (48).

$$\tau_{xx} = \frac{2}{3}\mu\left(2\frac{\partial u}{\partial x} - \frac{\partial v}{\partial y}\right), \tau_{yy} = \frac{2}{3}\mu\left(-\frac{\partial u}{\partial x} + 2\frac{\partial v}{\partial y}\right)$$
$$\tau_{xy} = \tau_{yx} = \mu\left(\frac{\partial u}{\partial y} + \frac{\partial v}{\partial x}\right) \tag{48}$$

The heat flux is calculated using Fourier's law as,

$$q_x = -k\frac{\partial \theta}{\partial x}, q_y = -k\frac{\partial \theta}{\partial y} \quad \text{with } k = \mu C_p/Pr \tag{49}$$

Where k is the thermal conductivity. The Prandtl number (Pr) is taken 0.72 (for air).

The second order fully implicit LU-SGS (Lower–Upper Symmetric Gauss–Seidel) backward A-stable scheme with a dual-time stepping is used for the time marching. The space discretization is done using forth order central finite volume scheme in a skew-symmetric form. The preconditioning method proposed in [26] to impose the incompressibility is used, for the flows at low speed (Mach number).

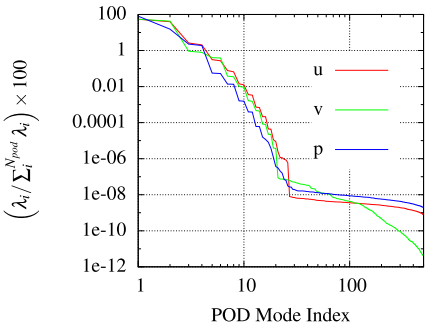

(a) % energy associated with each POD mode of u, v and p.

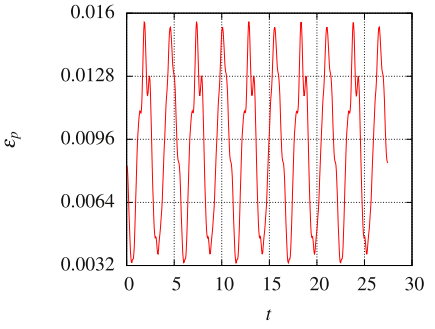

(b) The POD discretization error ($\epsilon_p(t; Re)$, as defined in Equation (30))

Fig. 2. POD analysis of the flow at $Re = 140$ (η).

3.2. Results and discussion

The state vector $\boldsymbol{s}$ in the case study (2-D, incompressible flow) can be considered as,

$$\boldsymbol{s}(\boldsymbol{x}, t; \eta) = \begin{pmatrix} u(\boldsymbol{x}, t; \eta) \\ v(\boldsymbol{x}, t; \eta) \\ p(\boldsymbol{x}, t; \eta) \end{pmatrix} \tag{50}$$

Where $\boldsymbol{x}$ is the space domain with x and y dimensions. t represents the time. The operating parameter η is the Reynolds number Re. The two reference cases are considered at Reynolds numbers $\eta_1 = Re_1 = 125$ and $\eta_2 = Re_2 = 150$. The number of snapshots taken for each reference case is $N_t = 900$, this constitutes ≈ 14 vortex shedding periods. The time step for snapshots collection is $\Delta t_{sn} = 0.05$. The correlation matrix was built for each reference case and solved for the eigenvalue problem as detailed in Section 2.1. The off-reference case is considered at $\eta = Re = 140$. The linear interpolation of the state vector time-averages and POD modes (both topos and chronos) using the reference states is performed as per Section 2.3. The results are build using first 10 POD modes ($N_r = 10$) out of 500 POD modes ($N_{pod} = 500$) and compared with the Navier–Stokes High Fidelity Model (HFM) simulation results at the same Reynolds number.

The results of POD analysis at $Re = 140$ are shown is Fig. 2, in terms of the eigenvalues and the time evolution of the discretization error involved in the method of snapshots POD. Fig. 2(a) shows the % energy associated with each POD mode of the state variables. It also indicates that the $\approx 99.99\%$ of total energy is contained in first 10 modes of each state variables. Therefore the number of reduced basis $N_r = 10$ is chosen for the interpolation (ROM). The discretization error in the method of snapshots POD ($\epsilon_p(t; \eta)$), as defined in Equation (30) is plotted in Fig. 2(b). The root-mean-squared (rms) of the error is $\approx 0.25\%$ of the variance of the state variable.

3.2.1. Interpolation of the POD reduced basis

In this case study, the POD space modes ($\boldsymbol{\phi}_i(\boldsymbol{x}; \eta)$) are either symmetric or antisymmetric about the x axis. The pre-conditioning in Equation (22) is needed for the antisymmetric modes, only when they observe a flip of sign in changing operating condition (η). Fig. 3 shows the linear interpolation performed for the fifth space mode of the streamwise velocity (ϕ_5^u). Figs. 3(a) and 3(b) are the fifth POD space modes of the reference cases at $Re_1 = 125$ and $Re_2 = 150$ respectively. The result of interpolation at $Re = 140$ for $\phi_5^u(\boldsymbol{x}; Re)$ is shown in Fig. 3(d). Fig. 3(c) shows the actual POD mode (ϕ_5^u) at $Re = 140$, computed using the method of snapshots POD for comparison with the interpolated mode.

Similarly, the remaining topos from the reduced basis were interpolated at Reynolds number $Re = 140$. Fig. 4 shows comparison of the first four interpolated (ROM) modes (Figs. 4(b), 4(d), 4(f), 4(h)) versus the snapshots POD modes (Figs. 4(a), 4(c), 4(e), 4(g) respectively). One can notice that the POD modes act in pairs. The first pair of POD modes of streamwise velocity u (mode number 1 & 2) is antisymmetric, while the second one is symmetric about the x axis. In general here, the odd pairs of POD modes of u are antisymmetric and the even pairs are symmetric. The antisymmetry of the modes about x axis is dealt by the constrain in Equation (22) before interpolating the modes. The POD is a biorthogonal decomposition of the flow in space and time, there is one-to-one correspondence between topos and chronos [1]. The change in symmetry of a topo reflects in the corresponding chrono. Although this change of sign (of $\boldsymbol{\phi}_i$ and $\tilde{\boldsymbol{a}}_i$ for the same operating condition) does not alter the value of flow reconstruction by Equation (23). The phase information is anyway lost because of the second order statistics used in the POD basis functions [22]. In addition to the phase information, the change of operating condition (Re) leads to the change in orientation of the POD basis functions. The interpolation procedure ensures an appropriate orientation of the POD reduced basis for an intermediate operating conditions between the reference states.

In Galerkin ROMs the time coefficients often need corrections in their amplitudes. The common source of error is due to the truncation of higher POD modes and the formulation of the ROM without pressure-term representation. For instance, the Galerkin ROMs without pressure-term consideration leads to higher amplitudes of the POD time coefficients [18]. The

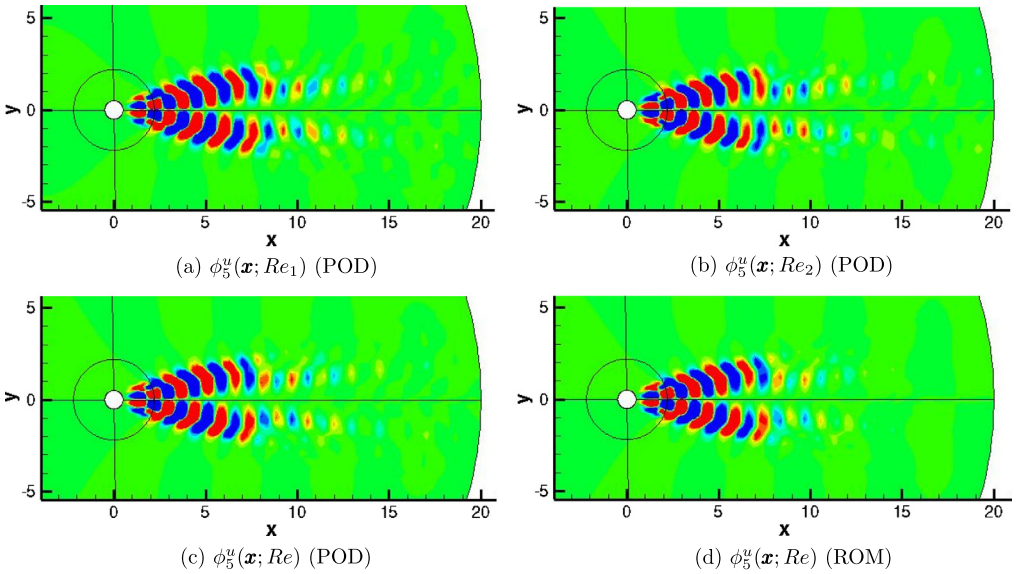

Fig. 3. Interpolation of $\phi_5^u(\boldsymbol{x}, \cdot)$.

characteristic POD time coefficients ($\tilde{\boldsymbol{a}}_i(t; Re)$) are immune from the truncation and pressure-term errors, since they are extracted from the time coefficients of the POD ($\boldsymbol{a}_i(t; Re)$) itself as per Equation (18) for the reference cases (η_1 and η_2). The characteristic time coefficients, similar to the fellow spacial modes act in pairs. The interpolation results for the characteristic time coefficients (chronos) are shown in Fig. 5. It shows the comparison of interpolation results in phase space for the first five characteristic time coefficients. The curves in each plot (Figs. 5(a), 5(b), 5(c) and 5(d)) expand in size, with the increase of Reynolds number. The limit-cycles represented in red color are for the reference state $Re_1 = 125$, while the ones in pink color are for the reference state $Re_2 = 150$. The limit-cycles at $Re = 140$, in blue color are interpolated using the reference states Re_1 and Re_2. It can be compared with the characteristic POD time modes obtained using snapshots POD at $Re = 140$ in green color.

In addition, the characteristic times (T_η) of the reference states $Re_1 = 125$ and $Re_2 = 150$ are $T_{Re_1} = 5.647$ and $T_{Re_2} = 5.400$ respectively. The linearly interpolated characteristic time at $Re = 140$ is $T_{Re} = 5.499$ against the value 5.489 obtained in POD analysis.

The eigenvalues of the interpolation ROM solution at $Re = 140$ were estimated using relation,

$$\boldsymbol{\lambda}_i = \left\langle \tilde{\boldsymbol{a}}_i(t; Re)^2 \right\rangle_{T_{Re}} \tag{51}$$

Fig. 6(a) shows the energy (in %) associated with the reduced interpolated (ROM) modes at $Re = 140$, it is compared with the energy (in %) of the corresponding snapshots POD modes (cumulative plot in Fig. 6(b)). The time-averaged flow energy estimation using the interpolated POD time modes (Equation (51)) evinces the orthogonality of the interpolated modes [3]. An additional orthogonality check is performed a posteriori on the interpolated reduced basis. The angle ($\theta_{\boldsymbol{\gamma},\boldsymbol{\beta}}$) between interpolated modes ($\boldsymbol{\gamma}, \boldsymbol{\beta} \in L^2(\Omega)$) is calculated by means of their inner product as,

$$\theta_{\boldsymbol{\gamma},\boldsymbol{\beta}} = \arccos\left(\frac{(\boldsymbol{\gamma}, \boldsymbol{\beta})_\Omega}{||\boldsymbol{\gamma}||_\Omega ||\boldsymbol{\beta}||_\Omega}\right) \tag{52}$$

The angles (in degree) between the interpolated reduced basis of streamwise velocity (u) are tabulated in Table 1. It clearly demonstrates that the interpolation of the POD modes retains the orthogonality of both the topos ($\boldsymbol{\phi}_i$) and chronos ($\tilde{\boldsymbol{a}}_i$).

The errors quantification, as formulated in Section 2.4 is plotted in Fig. 7. The truncation error ($\epsilon_t(t; Re)$) is nothing but the contribution of higher order POD basis functions ($N_{pod} - N_r$) to the fluctuations in state variables. The maximum truncation error is $\approx 0.25\%$ of the variance (σ^2) for each state variable (Fig. 7(a)). The interpolation error ($\epsilon_i(t; Re)$) is relatively high, the maximum of it is about 2% of the variance, for $\Delta\eta = \Delta Re = 25$. The total error relevant to the interpolation ROM ($\epsilon_{it}(t; Re)$) is also ~ 10 times the truncation error. Fig. 7(b) shows the errors (ϵ_i, ϵ_t & ϵ_{it}) in phase space. The limit cycles illustrate the boundedness of errors amplitude with the time evolution. On the other hand, maximum of the energy based error $\epsilon_e(t; Re)$ (as defined in Equation (40)) is $\approx 22\%$ of the variance (Fig. 7(c)). Further, the phase diagrams in Fig. 7(b) and Fig. 7 (d) show that the errors follow the stable limit cycles, demonstrating the stability of interpolation ROM method.

3.2.2. High fidelity solution comparisons

Fig. 8(a) shows the average of streamwise velocity $\bar{u}(\boldsymbol{x}; Re)$ obtained using the high fidelity computational fluid dynamics (CFD) simulation at Reynolds number $Re = 140$. The interpolated time-average of the streamwise velocity at same Reynolds

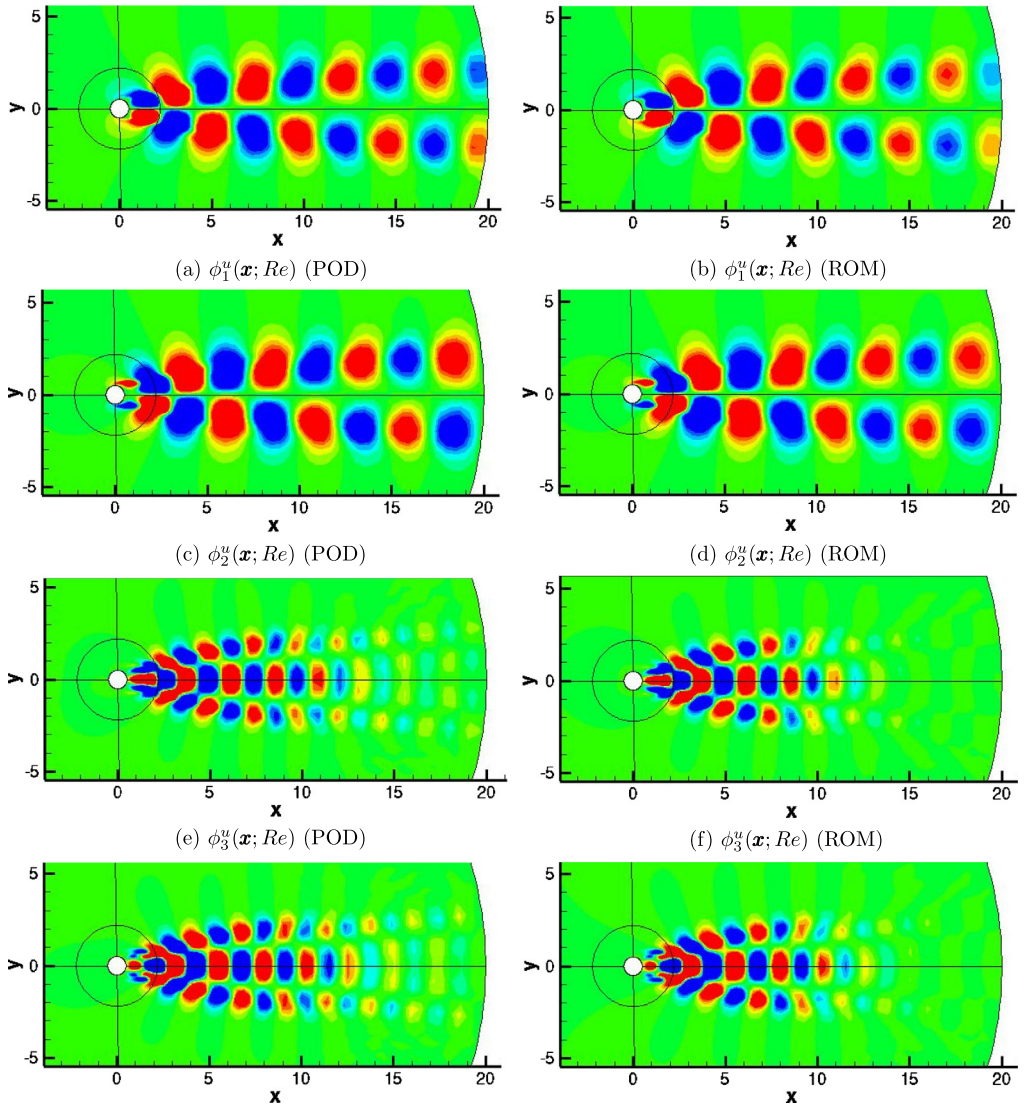

(a) $\phi_1^u(\boldsymbol{x}; Re)$ (POD) (b) $\phi_1^u(\boldsymbol{x}; Re)$ (ROM)

(c) $\phi_2^u(\boldsymbol{x}; Re)$ (POD) (d) $\phi_2^u(\boldsymbol{x}; Re)$ (ROM)

(e) $\phi_3^u(\boldsymbol{x}; Re)$ (POD) (f) $\phi_3^u(\boldsymbol{x}; Re)$ (ROM)

(g) $\phi_4^u(\boldsymbol{x}; Re)$ (POD) (h) $\phi_4^u(\boldsymbol{x}; Re)$ (ROM)

Fig. 4. Comparison of $\phi_1^u(\boldsymbol{x}, Re)$ to $\phi_4^u(\boldsymbol{x}, Re)$ modes obtained by the snapshots POD against the modes obtained using linear interpolation (ROM) at $Re = 140$.

Table 1
Orthogonality (angle between the modes in degree) of the interpolated reduced basis.

	ϕ_1^u	ϕ_2^u	ϕ_3^u	ϕ_4^u	ϕ_5^u	ϕ_6^u	ϕ_7^u	ϕ_8^u	ϕ_9^u	ϕ_{10}^u
ϕ_1^u	00.0	89.9	89.9	90.4	90.1	90.0	90.0	90.0	90.0	90.1
ϕ_2^u	89.9	00.0	90.4	90.1	89.8	90.0	90.0	90.0	90.0	90.0
ϕ_3^u	89.9	90.4	00.0	90.4	89.8	90.5	90.1	89.9	90.0	90.0
ϕ_4^u	90.4	90.2	90.4	00.0	90.5	90.3	90.1	89.8	90.0	90.0
ϕ_5^u	90.1	89.8	89.8	90.5	00.0	89.8	90.3	89.7	90.5	89.9
	$\tilde{a}_1^u$	$\tilde{a}_2^u$	$\tilde{a}_3^u$	$\tilde{a}_4^u$	$\tilde{a}_5^u$	$\tilde{a}_6^u$	$\tilde{a}_7^u$	$\tilde{a}_8^u$	$\tilde{a}_9^u$	$\tilde{a}_{10}^u$
$\tilde{a}_1^u$	00.0	90.1	89.0	89.3	90.2	89.7	89.5	90.4	90.4	90.3
$\tilde{a}_2^u$	90.1	00.0	88.7	90.3	91.6	91.3	90.1	90.5	90.3	88.3
$\tilde{a}_3^u$	89.0	88.7	00.0	90.5	91.7	88.3	90.2	88.0	90.3	89.7
$\tilde{a}_4^u$	89.3	90.3	90.5	00.0	88.1	88.0	90.8	89.6	89.6	91.0
$\tilde{a}_5^u$	90.2	91.6	91.7	88.1	00.0	89.9	87.8	94.0	91.4	90.3

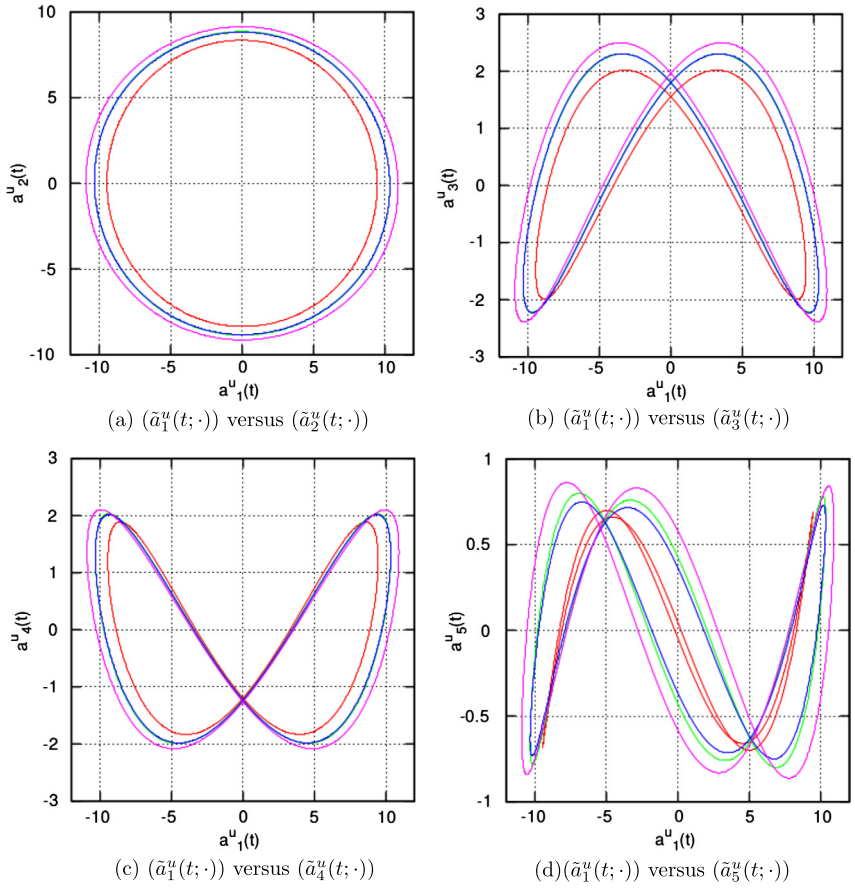

(a) $(\tilde{a}_1^u(t;\cdot))$ versus $(\tilde{a}_2^u(t;\cdot))$ (b) $(\tilde{a}_1^u(t;\cdot))$ versus $(\tilde{a}_3^u(t;\cdot))$

(c) $(\tilde{a}_1^u(t;\cdot))$ versus $(\tilde{a}_4^u(t;\cdot))$ (d)$(\tilde{a}_1^u(t;\cdot))$ versus $(\tilde{a}_5^u(t;\cdot))$

Fig. 5. Comparison of the time coefficients $\tilde{a}_i^u(T.;\cdot)$ of the first five chronos. The blue curve in each plot is an interpolated mode (ROM) at $Re = 140$ against the snapshot POD mode at $Re = 140$ in green. The other color correspondence with Reynolds numbers is: Red $\rightarrow Re_1 = 125$ and Pink $\rightarrow Re_2 = 150$. (For interpretation of the references to color in this figure legend, the reader is referred to the web version of this article.)

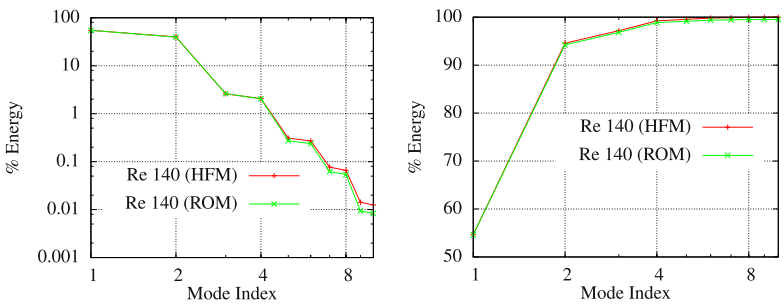

(a) Energy (eigen values) comparison (b) Cumulative energy comparison

Fig. 6. Energy comparison of the interpolated (ROM) modes with the snapshots POD modes.

number ($Re = 140$) using the reference states at $Re = 125$ and $Re = 150$ is shown in Fig. 8(b). Generally, the time-averaged base flow shows little variation over the long range of Reynolds numbers. In addition, the dimensionless quantities of practical importance such as Drag, Lift coefficients vary with the logarithmic change in Reynolds number. Therefore the second derivatives $\boldsymbol{\alpha}_*$ in Equation (38), contributing to the error bounds for the interpolation error can be expected to be small, providing the possibility to have larger $\Delta\eta$. Fig. 9(a) shows the phase plot of the Drag versus Lift coefficients estimated using pressure force, for both the high fidelity (HFM) and interpolation ROM solutions at $Re = 140$. Fig. 9(b) shows the comparison of time-averaged pressure coefficient profile on the surface of cylinder at $Re = 140$. The Drag, Lift and pressure coefficients are estimated (respectively) as,

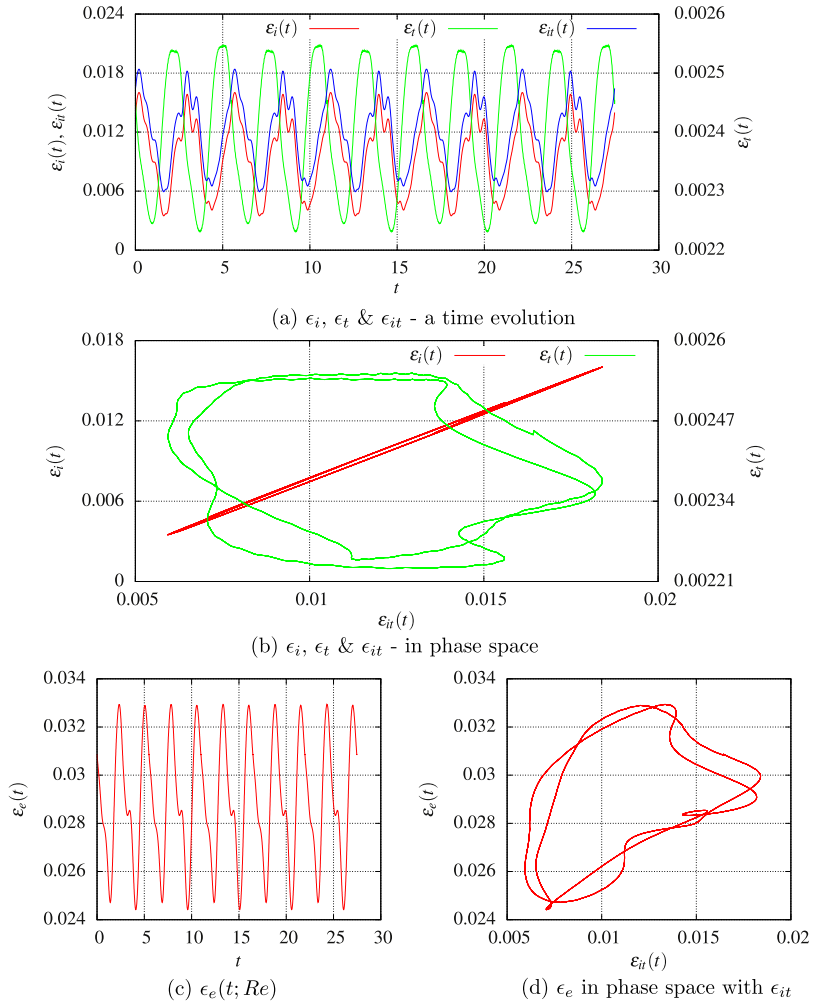

(a) ϵ_i, ϵ_t & ϵ_{it} - a time evolution

(b) ϵ_i, ϵ_t & ϵ_{it} - in phase space

(c) $\epsilon_e(t; Re)$

(d) ϵ_e in phase space with ϵ_{it}

Fig. 7. Time evolution and phase diagrams of the errors.

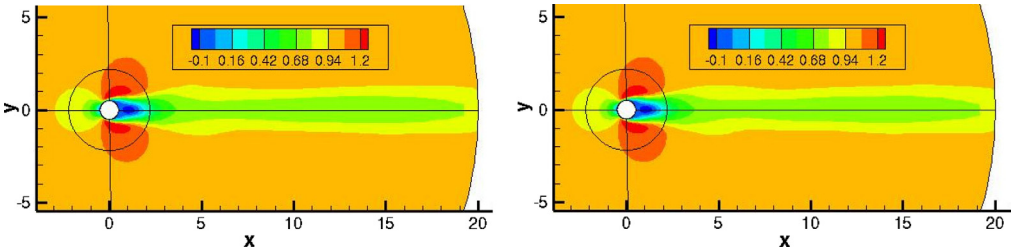

(a) $\bar{u}(\boldsymbol{x}; Re)$ (HFM)

(b) $\bar{u}(\boldsymbol{x}; Re)$ (ROM)

Fig. 8. Time-averaged base flow comparison at $Re = 140$ ($\bar{u}(\boldsymbol{x}, Re)$).

$$C_d = 2\int_{L_p} p_l \hat{x} dl; \quad C_l = 2\int_{L_p} p_l \hat{y} dl \quad \text{and} \quad C_p = 2(p - p_\infty) \tag{53}$$

Where L_p is the perimeter of cylinder, p_l is the pressure on the small segment (dl) of the perimeter. $\hat{x}$, $\hat{y}$ are the projections of the unit vector normal to a length segment dl along the inflow (x) and flow normal (y) directions respectively.

The time signal of streamwise velocity in Fig. 10(a) is probed at $x = 5$, $y = 0$. The time evolution of the Drag and Lift coefficients for unit cylinder length (estimated using pressure force only) is compared in Fig. 10(b). It shows a fairly good agreement with the high fidelity CFD simulation results. The ROM time signals are $\sim$27 T_{Re} long and they persist for any time duration (T_∞).

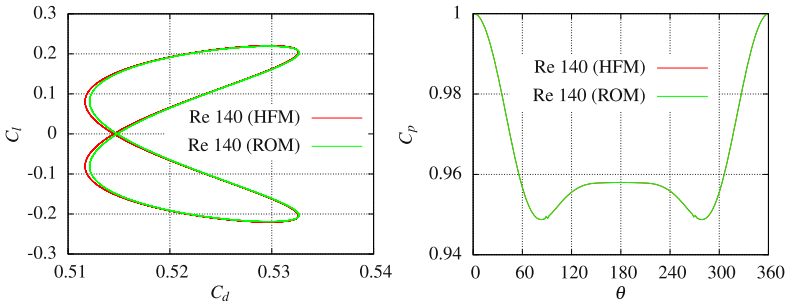

(a) Drag versus Lift coeff. comparison (b) Time-averaged pressure profile

Fig. 9. Phase plot of drag vs lift coeff. and surface pressure profile comparison.

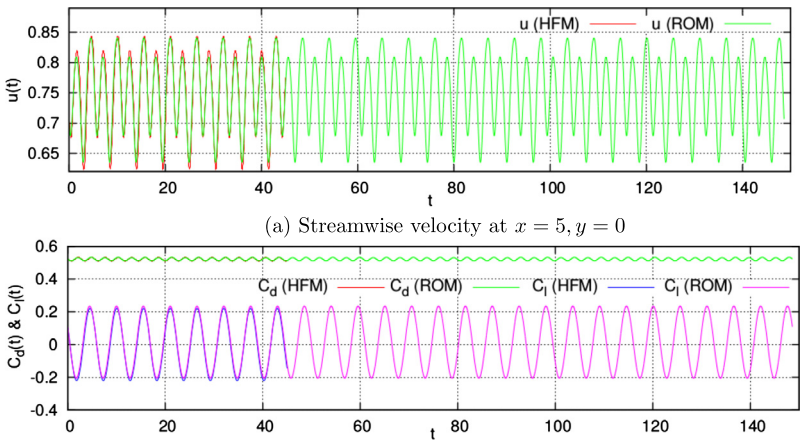

(a) Streamwise velocity at $x = 5, y = 0$

(b) Drag and Lift (pressure) force coeff.

Fig. 10. Comparison of time signals of u, C_d and C_l.

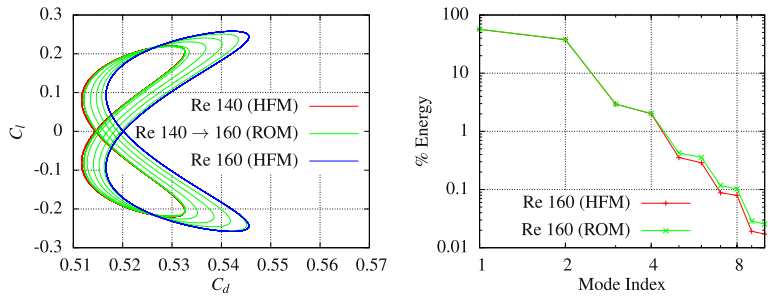

(a) $C_d(t)$ Vs $C_l(t)$ (b) Energy comparison

Fig. 11. (a) Drag vs Lift coeff. plot showing a smooth transition from $Re = 140$ to $Re = 160$ and (b) energy comparison between HFM ($Re = 160$) and the ROM solution ($Re = 160$) built using a linear extrapolation.

A smooth transition between the two off-reference ROM solution is shown in Fig. 11 (a). The figure shows the drag and lift coefficients plot. The continuous transition of the ROM solution states from $Re = 140$ to $Re = 160$ is obtained by using Equations (24), (25) and (26). The time coefficient parameter in Equation (26) is taken as $c_\tau \approx 0.27$, in order to have the transition between the two operating conditions in 20 s. The value of c_τ varies linearly with time period $T_{\eta^{n+1}}$, for a fixed input of the transition time. The ROM solution at an off-reference operating condition ($Re = 160$) is computed by using a linear extrapolation of the reference solution states at $Re = 125$ and $Re = 150$. The result of linear extrapolation are compared in Fig. 11(b), in terms of the % of streamwise velocity (u) fluctuations captured. The plot shows that the ROM solution captures $\approx 98\%$ of the streamwise energy accurately.

4. Summary

A simple and robust approach to the model reduction of Navier–Stokes equations is presented. In contrast to the Galerkin Reduced-Order Models (ROMs), the method is based on the periodicity of the Proper Orthogonal Decomposition (POD) time coefficients – a beautiful feature of the POD temporal basis functions (chronos) – in statistically stationary flows. In order to cope with the changing operating condition (such as Reynolds number) the reduced POD basis is interpolated using a linear interpolation of the reference operating conditions. The error and stability analysis suggests that the errors in the snapshots POD, truncation of the higher order POD modes and the linear interpolation are bounded for the time evolution. The total absolute error mainly depends on the difference in the two reference states ($\Delta\eta$) and a sensitivity of the flow to the operating parameter. The results of high fidelity CFD simulation of the flow past a cylinder show good agreement with the proposed method. The stable limit-cycles of the errors and the linear interpolation of reduced basis for changing operating condition ensure respectively the stability and robustness of the interpolation ROM. Although the considered case study is in 2-dimensional (2-D) and for an incompressible flow, the mathematical formulation is developed for the full 3-D compressible Navier–Stokes equations. Further, each state variable is treated independently, therefore we anticipate the applicability of the method for a wide range of the problems with coupled phenomena (e.g. flow around aerofoil at high Mach, fluid–structure interaction).

Acknowledgement

The authors acknowledge Centre National de la Recherche Scientifique (CNRS) for facilitating the work via Agence Nationale de la Recherche (ANR-11-MONU-0004) project Baresafe. The authors would like to thank Dr. Rémi Bourguet of Massachusetts Institute of Technology – MIT for his suggestions during this research.

References

[1] N. Aubry, On the hidden beauty of the proper orthogonal decomposition, Theor. Comput. Fluid Dyn. 2 (1991) 339–352.
[2] N. Aubry, P. Holmes, J.L. Lumley, E. Stone, The dynamics of coherent structures in the wall region of a turbulent boundary layer, J. Fluid Mech. 192 (1988) 115–173.
[3] M. Balajewicz, E. Dowell, Stabilization of projection-based reduced order models of the Navier–Stokes, Nonlinear Dyn. 70 (2012) 1619–1632.
[4] D. Barkley, R.D. Henderson, Three-dimensional Floquet stability analysis of the wake of a circular cylinder, J. Fluid Mech. 322 (1996) 215–241.
[5] M. Bergmann, C.H. Bruneau, A. Iollo, Enablers for robust POD models, J. Comput. Phys. 228 (2009) 516–538.
[6] J. Demmel, Applied Numerical Linear Algebra, Society for Industrial and Applied Mathematics, 1997.
[7] A. Dumon, C. Allery, A. Ammar, Proper generalized decomposition method for incompressible Navier–Stokes equations with a spectral discretization, Appl. Math. Comput. 219 (2013) 8145–8162.
[8] P. Holmes, G. Berkooz, J.L. Lumley, Turbulence, dynamical systems and the unreasonable effectiveness of empirical eigenfunctions, in: Proceedings of the International Congress of Mathematicians, Kyoto, 1990, pp. 1607–1617.
[9] D.D. Joseph, Stability of fluid motions. I, II, NASA STI/Recon technical report A 77, 1976, 12423.
[10] K. Kunisch, S. Volkwein, Galerkin proper orthogonal decomposition methods for a general equation in fluid dynamics, SIAM J. Numer. Anal. 40 (2002) 492–515.
[11] T.M. Lassila, A. Manzoni, A. Quarteroni, G. Rozza, Model order reduction in fluid dynamics: challenges and perspectives, in: A. Quarteroni, G. Rozza (Eds.), Reduced Order Methods for Modeling and Computational Reduction, in: MS&A, Springer, Milano, 2013, pp. 235–273, EPFL MATHICSE report 22.2013.
[12] J.L. Lumley, The structure of inhomogeneous turbulent flows, in: A.M. Yaglom, V.I. Tatarski (Eds.), Atmospheric Turbulence and Radio Propagation, Nauka, Moscow, 1967, pp. 166–178.
[13] X. Ma, G.E. Karniadakis, A low-dimensional model for simulating three-dimensional cylinder flow, J. Fluid Mech. 458 (2002) 181–190.
[14] M. Morzynski, W. Stankiewicz, B.R. Noack, F. Thiele, R. King, G. Tadmor, Generalized mean-field model for flow control using a continuous mode interpolation, in: Proceedings of the Third AIAA Flow Control Conference, 2006, pp. 1–11.
[15] B.R. Noack, K. Afanasiev, M. Morzynski, G. Tadmor, F. Thiele, A hierarchy of low-dimensional models for the transient and post-transient cylinder wake, J. Fluid Mech. 497 (2003) 335–363.
[16] B.R. Noack, H. Eckelmann, A low-dimensional Galerkin method for the three-dimensional flow around a circular cylinder, Phys. Fluids 6 (1994) 124–143.
[17] B.R. Noack, M. Morzynski, G. Tadmor, Reduced-Order Modelling for Flow Control, vol. 528, Springer, 2011.
[18] B.R. Noack, P. Papas, P.A. Monkewitz, The need for a pressure-term representation in empirical Galerkin models of incompressible shear flows, J. Fluid Mech. 523 (2005) 339–365.
[19] D. Rempfer, On low-dimensional Galerkin models for fluid flow, Theor. Comput. Fluid Dyn. 14 (2000) 75–88.
[20] C.W. Rowley, T. Colonius, R.M. Murray, Model reduction for compressible flows using POD and Galerkin projection, Physica D: Nonlinear Phenom. 189 (2004) 115–129.
[21] C.W. Rowley, I. Mezić, S. Bagheri, P. Schlatter, D.S. Henningson, Spectral analysis of nonlinear flows, J. Fluid Mech. 641 (2009) 115–127.
[22] P.J. Schmid, Dynamic mode decomposition of numerical and experimental data, J. Fluid Mech. 656 (2010) 5–28.
[23] S. Sirisup, G. Karniadakis, A spectral viscosity method for correcting the long-term behavior of POD models, J. Comput. Phys. 194 (2004) 92–116.
[24] S. Sirisup, G. Karniadakis, Stability and accuracy of periodic flow solutions obtained by a POD-penalty method, Physica D: Nonlinear Phenom. 202 (2005) 218–237.
[25] L. Sirovich, Turbulence and the dynamics of coherent structures. Part I: coherent structures, Q. Appl. Math. XLV (1987) 561–571.
[26] E. Turkel, V.N. Vatsa, R. Radespiel, Preconditioning methods for low-speed flows, National Aeronautics and Space Administration, 1996. NASA CR 201605.